Active Metasurface-Based Reconfigurable Polarization Converter With Multiple and Simultaneous Functionalities

Samiran Pramanik, *Student Member, IEEE*, Saikat Chandra Bakshi, *Member, IEEE*, Chaitali Koley, *Member, IEEE*, Debasis Mitra, *Member, IEEE*, Alessio Monti, *Senior Member, IEEE*, and Filiberto Bilotti, *Fellow, IEEE*

***Abstract*—We introduce a new concept of three-states polarization converting metasurface (TS-PCM) based on p-i-n diodes. The proposed structure can offer three distinct wave manipulation functionalities: linear polarization to orthogonal linear polarization (LP-OLP), linear polarization to circular polarization (LP-CP), and linear polarization to full reflection (LP-FR) state. Unlike previous structures, the multiple conversion features are simultaneously achieved in different frequency ranges, depending on the operating state of diode (OFF or ON). Finally, a sample prototype was fabricated and the experimental results were verified with the simulated ones.**

***Index Terms*—Active metasurface, linear polarization and circular polarization (LP and CP), p-i-n diodes, polarization converter.**

I. Introduction

POLARIZATION converters play a key role in reconfigurable and stealth antennas, radar cross section (RCS) reduction, and wave-manipulation applications [1], [2], [3]. Aiming various types of application demands, two main types of polarization converters were developed, namely (1) linear to orthogonal linear polarization (LP-OLP) converters [4], [5], [6], [7], and (2) linear to circular polarization (LP-CP) [8], [9], [10]. However, the capability of the designs [4], [5], [6], [7], [8], [9], [10] are limited, as they can offer only a single functionality (either LP-OLP or LP-CP) at a time. Although simultaneous conversion (LP–OLP and LP-CP) is achieved [11], [12], [13], [14], such structures exhibited fixed functionalities and, thus, the operating conversion states (i.e., LP-OLP or LP-CP) could not be selected after fabrication.

To mitigate these issues, switchable polarization converters were introduced [15], [16], [17], [18], [19], [20]. For example, in [15], the operating mode (either LP-OLP or LP-CP) is selected by using a MEMS switch. The design proposed in [16] offers a selection option between LP-CP and no conversion state. Similarly, switchable LP-OLP and LP-FR (FR: full reflection) state is achieved in [17]. In [18], by controlling the reverse bias voltage of varactor diodes, LP-OLP and LP-CP are achieved at 0 V and -19 V, respectively. However, both types of switchable conversion states (LP-OLP and LP-CP) are not achieved simultaneously. Very recently, in [19], by varying the properties of a solid-state plasma LP-OLP and LP-CP conversions have been demonstrated, but the used technology is rather complicated and costly.

In this letter, a three-state polarization converting metasurface (TS-PCM) is presented to achieve LP-OLP, LP-CP, and LP-FR functionalities. In the OFF state of p-i-n diodes, the structure offers two distinct operating modes, i.e., LP-CP and LP-FR. Conversely, when the diodes are switched ON, the device offers two distinct LP-OLP and LP-CP modes. Moreover, switchable LP-CP conversion is also achieved in two different modes at separate frequency bands to enhance the applicability of the device in real scenarios.

II. Design and Analysis

A. Geometrical Configuration

The geometry of the proposed TS-PCM consisting of slot-loaded rotated rectangular ring is illustrated in Fig. 1, where p-i-n diodes are modeled according to their datasheet/characterization [21]. Two separate cut wires oriented $+45^\circ$ w.r.t. the x-axis are purposefully included in the unit-cell to introduce an additional capacitive effect. The design of the unit-cell is carefully chosen so that it can also fit with an efficient biasing strategy, by incorporating the bias lines and vias.

B. Working Principle

The unit-cell (see Fig. 1), is simulated in ANSYS HFSS using master/slave boundary conditions and Floquet ports excitation.

Manuscript received 19 July 2022; revised 13 September 2022; accepted 15 September 2022. Date of publication 1 November 2022; date of current version 3 March 2023. *(Samiran Pramanik and Saikat Chandra Bakshi contributed equally to this work.) (Corresponding author: Samiran Pramanik.)*

Samiran Pramanik and Chaitali Koley are with the Electronics and Communication Engineering Department, National Institute of Technology Mizoram, Chaltlang 796012, India (e-mail: pramaniksamiran@gmail.com; chaitali.ece@nitmz.ac.in).

Saikat Chandra Bakshi is with the Electrical and Computer Engineering Department, National University of Singapore, Singapore 117583 (e-mail: saikat@nus.edu.sg).

Debasis Mitra is with the Electronics and Telecommunication Engineering Department, Indian Institute of Engineering Science and Technology, Shibpur, Howrah 711103, India (e-mail: debasisiit@gmail.com).

Alessio Monti and Filiberto Bilotti are with the Department of Industrial, Electronic and Mechanical Engineering, Roma Tre University, 00146 Rome, Italy (e-mail: alessio.monti@uniroma3.it; filiberto.bilotti@uniroma3.it).

Digital Object Identifier 10.1109/LAWP.2022.3217130

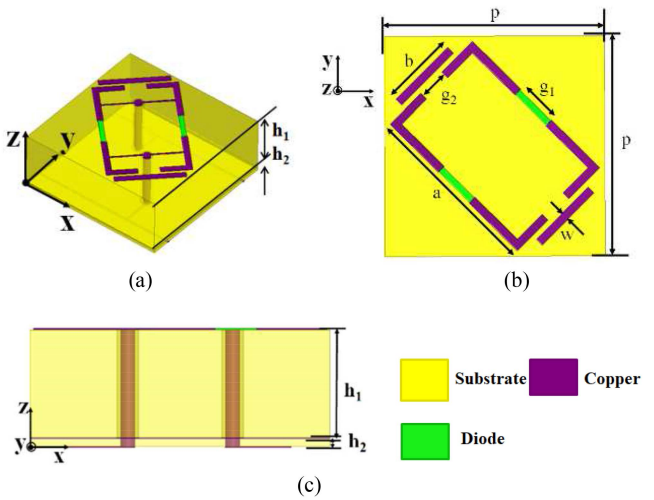

Fig. 1. Structure of the reconfigurable TS-PCM (a) perspective view of the unit-cell, (b) top view of the unit-cell with the relevant geometrical parameters, and (c) side view of the unit-cell (The parameters are: $P = 15$ mm, $g_1 = 1.6$ mm, $g_2 = 1.5$ mm, $h_1 = 5.4$ mm, $h_2 = 0.2$ mm, $a = 8.48$ mm, $b = 2.83$ mm, and $w = 0.5$ mm).

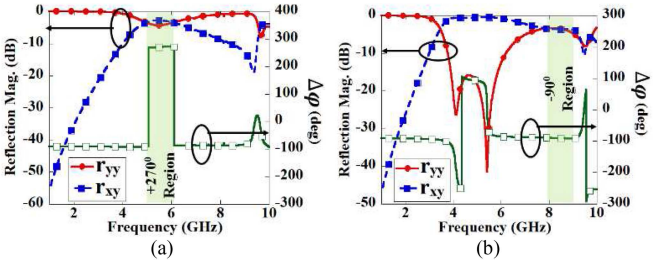

Fig. 2. Simulated co- and cross-polarization reflection magnitude (mag.) and phase difference of the designed unit-cell for a normally incident y-polarized wave when (a) diodes are OFF and (b) diodes are ON. (To describe the conversion characteristics of the TS-PCM when illuminated by a y-polarized incident wave, we define $r_{yy} = \frac{|\vec{E}_y^r|}{|\vec{E}_y^i|}$ and $r_{xy} = \frac{|\vec{E}_x^r|}{|\vec{E}_y^i|}$ as co-polarization (y-to-y) and cross-polarization (y-to-x) reflection magnitudes, respectively).

It can be observed from Fig. 2(a) that, in the frequency range 5.20–6.10 GHz, the reflection magnitudes r_{yy} and r_{xy} are almost equal to -3 dB. Whereas, the magnitude of r_{yy} is above -1 dB in the frequency range 2–3.66 GHz and 8.42–9.52 GHz, with the magnitude of r_{xy} in the same both range are below -10 dB. These two results indicate that, when both diodes are in the OFF state, the designed TS-PCM generates a CP wave in a single frequency band while working as an LP wave reflector [22] in the two different frequency bands.

For the ON state of the diodes, a -10 dB reduction of r_{yy} is observed [see Fig. 2(b)] in the range 3.77–6.20 GHz, where r_{xy} is above -1 dB throughout the band. Additionally, it can be noted that, in the upper frequency band 7.75–8.60 GHz, the reflection magnitudes r_{yy} and r_{xy} are almost equal (-3 dB), resulting in the generation of a CP wave. This indicates that, when both the diodes are in the ON state, the designed TS-PCM simultaneously generates a cross-polarized wave (3.77–6.20 GHz) and left-handed CP wave (7.75–8.60 GHz) for normally incident y-polarized wave.

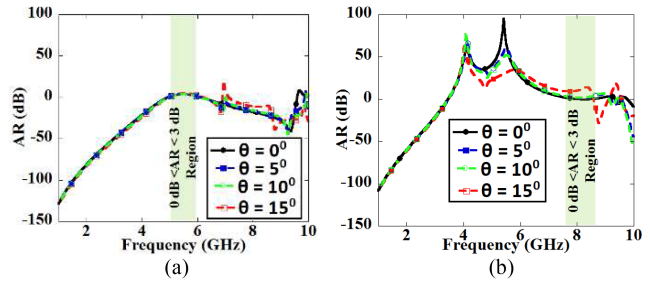

Fig. 3. Simulated AR for different oblique incident angles (θ) of a y-polarized incident wave when (a) the diodes are OFF and (b) the diodes are ON.

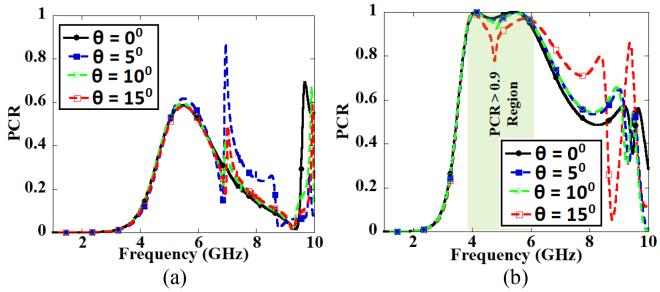

Fig. 4. Simulated PCR for different θ of a y-polarized incident wave when (a) the diodes are OFF and (b) the diodes are ON.

C. Performance Analysis

We start with the axial ratio (AR) parameter that is calculated as follows [23]:

$$AR = \left| \left(|r_{yy}|^2 + |r_{xy}|^2 + \sqrt{b} \right) / \left(|r_{yy}|^2 + |r_{xy}|^2 - \sqrt{b} \right) \right|^{1/2} \quad (1)$$

where

$$b = |r_{yy}|^4 + |r_{xy}|^4 + 2|r_{yy}|^2 |r_{xy}|^2 \cos(2 * \Delta\varphi)$$

and $\Delta\varphi = \varphi_{xy} - \varphi_{yy}$.

AR is reported in Fig. 3(a) and (b), during diodes are OFF and ON respectively. The AR is below 3 dB in the lower frequency band 5.20–6.10 GHz when the diodes are OFF, whereas it satisfies the same criteria in the band 7.75–8.60 GHz when the diodes are ON. These results confirm that the proposed TS-PCM behaves as an effective LP-CP converter within a frequency range that depends on the diode states. It can be further noted from Fig. 2 that the phase difference between the co- and cross-polarization reflection phases are approximately equal to $+270^\circ$ over the frequency band 5.20–6.10 GHz (when the diodes are OFF) and -90° in the frequency band 7.75–8.60 GHz (when the diodes are ON). The PCR parameter is defined [17] as $PCR_y = |r_{xy}|^2 / \left(|r_{xy}|^2 + |r_{yy}|^2 \right)$. It is also calculated and presented in Fig. 4. It can be observed that, when the diodes are OFF, PCR is less than 0.6 within the operating frequency range, i.e., no cross-polarization conversion takes place, except CP and FR. However, when the diodes are switched to the ON state, PCR is larger than 0.9 within the frequency range 3.77–6.20 GHz, indicating highly efficient LP-OLP conversion. Further, when the structure is simulated by launching obliquely incident

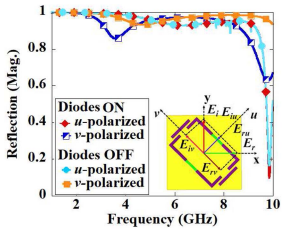

Fig. 5. Simulated reflection magnitudes of the unit-cell under u-v polarization.

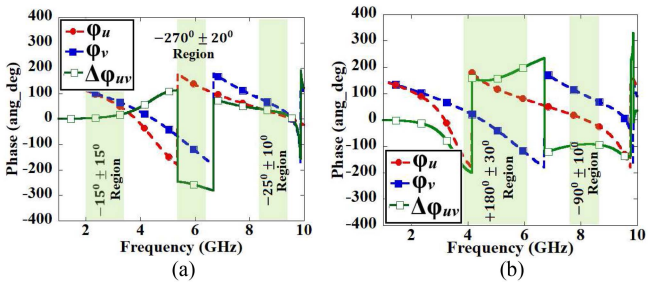

Fig. 6. Simulated reflection phase of the unit-cell under *u-v* polarization when (a) the diodes are OFF and (b) the diodes are ON.

EM PCR remains larger than 0.9 within the frequency range 3.80–6.17 GHz up to an incident angle of 10°.

III. Physical Mechanism Behind the TS-PCM Operation

This section aims to provide the physical insight on the operation of the TS-PCM. We provide the detailed analysis of the proposed structure from two different perspectives which are as follows.

A. Field Decomposition Along the U-V Axes

In particular, as shown in Fig. 5 (Inset), we define the uv axes along the $\pm 45^{\circ}$ directions in the xy plane. Electric field $(\vec{E}_{iy})$ of the y-polarized incident wave in this system is given by [14]

$$\vec{E}_{iy} = \frac{\sqrt{2}}{2} |E_0| e^{jkz} \vec{u} + \frac{\sqrt{2}}{2} |E_0| e^{jkz} \vec{v}. \tag{2}$$

Accordingly, the electric field $(\vec{E}_r)$ of the reflected wave is [14]

$$\vec{E}_r = \frac{\sqrt{2}}{2} |\Gamma_u| |E_0| e^{(-jkz+\varphi_u)} \vec{u} + \frac{\sqrt{2}}{2} |\Gamma_v| |E_0| e^{(-jkz+\varphi_v)} \vec{v}. \tag{3}$$

When the diodes are in the OFF state, the reflection magnitudes exhibit similar values in the frequency ranges 5.20–6.10 GHz, 2–3.66 GHz, and 8.42–9.52 GHz in Fig. 5. The reflection phase difference [in Fig. 6(a)] is roughly $+270^{\circ}$ in the frequency band 5.20–6.10 GHz (LP-CP conversion) whilst in the frequency bands 2–3.66 GHz, and 8.42–9.52 GHz, both ranges are neither $\pm 180^{\circ}$ nor $\pm 90^{\circ}$, indicating that the waves are reflected without any polarization conversion. However, when the diodes are switched ON, the reflection magnitudes along the *u-v* axes exhibit similar values in the frequency ranges 3.80–6.17 GHz and 7.75–8.60 GHz in Fig. 5. The reflection phase difference [in Fig. 6(b)] is nearly $+180^{\circ}$ in the lower frequency range 3.80–6.17 GHz (LP-OLP conversion) and around -90° in the higher frequency range 7.75–8.60 GHz (LP-CP conversion).

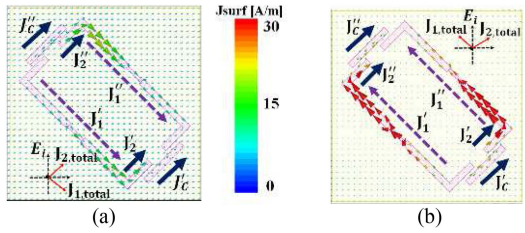

Fig. 7. Induced surface current distribution under a *y*-polarized incident wave for the LP-CP conversion when (a) the diodes are OFF and (b) the diodes are ON.

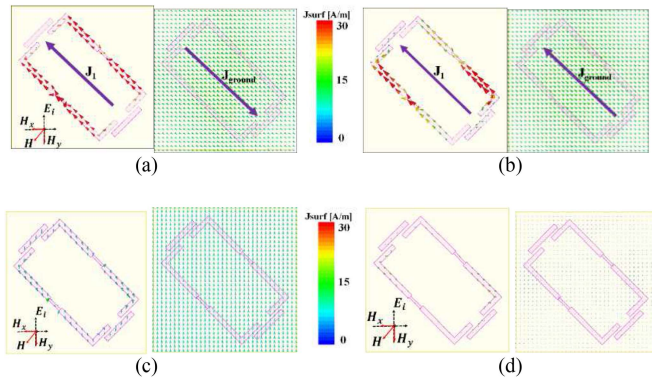

Fig. 8. Induced surface current distribution under a *y*-polarized incident wave at (a) 4.10 GHz, (b) 5.45 GHz for LP-OLP conversion mode, and (c) 2.83 GHz, (d) 8.97 GHz for LP-FR conversion mode.

B. Surface Current Distribution

In the OFF state, shown in Fig. 7(a), the current flow is evaluated at 5.65 GHz for LP-CP conversion and can be divided in two parts, (i) current flow in the up-down direction ($J_{1,\,\text{total}} = J_1^{'} + J_1^{''}$) and (ii) current flow in the left-right direction ($J_{2,\,\text{total}} = J_2^{'} + J_2^{''} + J_C^{'} + J_C^{''}$), being J_C the cut wire surface current density. Thus, the two flow directions are nearly orthogonal to each other. Next, the surface current distribution at the center frequency 8.17 GHz for the LP-CP polarization conversion when the diodes are in the ON state is presented. Again, as shown in Fig. 7(b), the net current flow consists of two orthogonal current paths, $(J_{1,\,\text{total}})$ and $(J_{2,\,\text{total}})$, (i) current flow in the up-down direction $(J_{1,\,\text{total}})$ and (ii) current flow consists of two orthogonal current paths, $(J_{1,\,\text{total}})$ and $(J_{2,\,\text{total}})$, (i) current flow in the up-down direction $(J_{1,\,\text{total}})$ and (ii) current flow in the left-right direction $(J_{2,\,\text{total}})$. Similarly, the flow directions are nearly orthogonal to each other which gives LP-CP conversion [14].

Further, the surface current distribution on the top metal and ground layers are reported in Fig. 8, at two resonant frequencies for the LP–OLP conversion when the diodes are ON. From Fig. 8(a), it can be observed that the surface currents (J_1) flow along the two arms of the split rectangular shaped resonator along the *v* direction at 4.10 GHz. The surface current density in the ground layer (J_{ground}) is in the opposite direction at this frequency. Hence an incident *y*-polarized incident field is converted

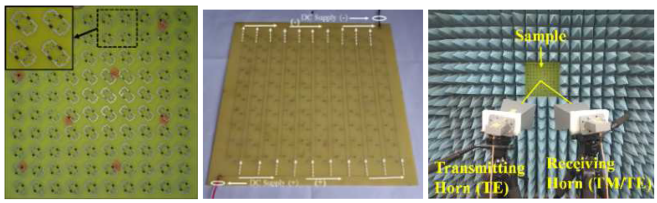

Fig. 9. Fabricated sample of manipulable TS-PCM. (a) Top layer, (b) biasing arrangement of bottom layer, and (c) schematic diagram for measurement setup.

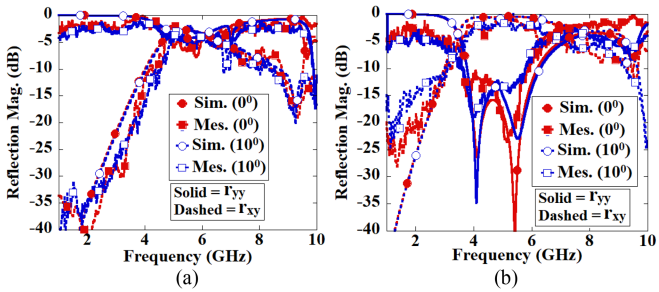

Fig. 10. Simulated and measured results of the fabricated sample when (a) the diodes are OFF and (b) the diodes are ON.

into an x-polarized reflected field [14]. From Fig. 8(b), we observe that at 5.45 GHz, the current densities in the top and ground layers flow nearly in the same direction, which corresponds to an electric dipole resonance. Thus, the x-component of the induced electric field is rotated into a cross-polarized component. Again, the surface current distributions are evaluated for LP-FR mode at 2.83 and 8.97 GHz when diodes are OFF in Fig. 8(c) and (d). It is observed that the top layer is not excited and extremely low current is distributed which is almost negligible. Hence, no conversion takes place, except copolarized reflection.

IV. Fabrication and Measurements

A prototype is fabricated using the PCB technique consisting of 10×10 unit-cells [see Fig. 1(a)] in Fig. 9 and tested using well-known free-space techniques [15], [17], [18] in Fig. 9(c). The p-i-n diodes from NXP (BAP 70-03 [21]) are mounted. The biasing methodology using dc lines and ac/dc isolation technique is similar [24], [25].

The measured and simulated results of the r_{yy} and r_{xy} reflection magnitudes are compared in Fig. 10. When all the diodes are OFF state, the designed sample returns LP-CP conversion over the frequency range 5.05–6.17 GHz and LP-FR conversion over the frequency ranges 2–3.66 GHz and 8.30–9.92 GHz. Conversely, when all the diodes are switched to ON state, the device behaves as an LP-OLP converter over the frequency range 3.77–6.00 GHz and as an LP-CP converter over the frequency range 7.35–8.15 GHz.

Further, when the structure is measured under an obliquely incident EM (Fig. 11) wave, all functionalities are found to be stable up to an incident angle of 10°. It can be observed that the phase difference is approximately equals to $+270° \pm 10°$ $(AR \leq 3\ dB)$ over the frequency band 5.17–5.99 GHz when

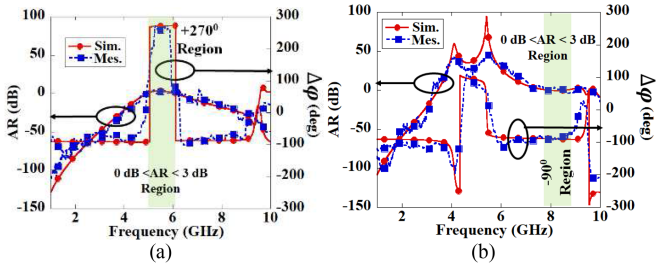

Fig. 11. Simulated and measured AR and phase difference $(\Delta\varphi)$ results of the fabricated sample when (a) the diodes are OFF, (b) the diodes are ON.

TABLE I
Performance Comparison of the Polarization Converter

Reference	P (mm) t (mm)	PC (Number of modes)	Number of A.C.	A.S.	RB (GHz)
[14] IET MAP	$0.33\lambda_C$ $0.111\lambda_C$	i) LP – OLP ii) LP – CP (Two)	N.A.	15^0	i) 7.74-14.44 (60.4%) ii) 14.95-17.35 (14.9%)
[17] AWPL	$0.34\lambda_C$ $0.096\lambda_C$	i) LP –OLP ii) LP – FR (Two)	2	15^0 (BW decreases.)	i) 3.39-5.01 (38%) ii) 3.83-4.74 (21%)
[26] TAP	$0.61\lambda_C$ $0.102\lambda_C$	i) LP – OLP or CP – CP (Two)	N.A.	15^0 (BW decreases.)	i) 10.2-20.5 (67.1%)
[27] MWCL	$0.33\lambda_C$ $0.081\lambda_C$	i) LP – CP ii) LP – OLP (Two)	1	10^0 (BW decreases.)	i) 11.8-24.1 (68.5%) ii) 10.5-13.9 (27.9%) iii) 17.7-27.2 (42.32%)
Our Work	$\mathbf{0.23\lambda_C}$ $\mathbf{0.089\lambda_C}$	**i) LP – OLP ii) LP – CP iii) LP – FR** (Three)	**2**	$0 - 10^0$	**i) 3.77-6.20 (48.8%) ii) 7.75-8.6 (10.4%) iii) 5.20-6.10 (16%) iv) 8.42-9.52 (13.3%) v) 2-3.66 (58.7%)**

RB: Relative Bandwidth over PCR > 90% (LP-OLP) or AR < 3dB (LP-CP), λ_C indicates the wavelength at the center frequency of the lower frequency band, P: Unit-cell size (lateral dimension), t: Thickness of substrate, PC: Polarization conversion, BW: Bandwidth, A.C: Active Components, and A.S.: Angular Stability.

the diodes are OFF, and $-90° \pm 10°$ $AR \leq 3$ dB) in the frequency band 7.75–8.47 GHz when the diodes are ON. Finally, a comparison with the state of the art is carried out and presented in Table I. Additionally, our proposed device is targeted to match the operating frequency bands for various application purposes [28], [29], [30], [31].

V. Conclusion

In this letter, a reconfigurable TS-PCM is designed, analyzed and experimentally tested. The proposed device is expected to find applications in reconfigurable devices, RCS reduction and also in polarization control devices.

References

[1] C. Holloway, E. Kuester, J. Gordon, J. O'Hara, J. Booth, and D. Smith, "An overview of the theory and applications of metasurfaces: The two-dimensional equivalents of metamaterials," *IEEE Antennas Propag. Mag.*, vol. 54, no. 2, pp. 10–35, Apr. 2012.

[2] Y. Liu, Y. Hao, K. Li, and S. Gong, "Radar cross section reduction of a microstrip antenna based on polarization conversion metamaterial," *IEEE Antennas Wireless Propag. Lett.*, vol. 15, pp. 80–83, 2016, doi: 10.1109/LAWP.2015.2430363.

[3] C. Ni, M. Chen, Z. Zhang, and X. Wu, "Design of frequency-and polarization-reconfigurable antenna based on the polarization conversion metasurface," *IEEE Antennas Wireless Propag. Lett.*, vol. 17, no. 1, pp. 78–81, Jan. 2018.

[4] X. Gao, X. Han, W. Cao, H. Li, H. Ma, and T. Cui, "Ultrawideband and high-efficiency linear polarization converter based on double V shaped metasurface," *IEEE Trans. Antennas Propag.*, vol. 63, no. 8, pp. 3522–3530, Aug. 2015.

[5] D. Tian et al., "Broadband asymmetric transmission of linearly polarised wave based on bilayered chiral metamaterial," *IET Microw., Antennas Propag.*, vol. 11, no. 2, pp. 171–176, 2017, doi: 10.1049/iet-map.2016.0342.

[6] H. Sun, C. Gu, X. Chen, Z. Li, L. Liu, and F. Martín, "Ultra-wideband and broad-angle linear polarization conversion metasurface," *J. Appl. Phys.*, vol. 121, no. 17, 2017, Art. no. 174902.

[7] G. Deng, H. Sun, K. Lv, J. Yang, Z. Yin, and B. Chi, "An efficient wideband cross-polarization converter manufactured by stacking metal/dielectric multilayers via 3D printing," *J. Appl. Phys.*, vol. 127, no. 9, 2020, Art. no. 093103.

[8] J. Baena, S. Glybovski, J. del Risco, A. Slobozhanyuk, and P. Belov, "Broadband and thin linear-to-circular polarizers based on self-complementary zigzag metasurfaces," *IEEE Trans. Antennas Propag.*, vol. 65, no. 8, pp. 4124–4133, Aug. 2017.

[9] Y. Jia et al., "Ultrawideband metasurface with linear-to-circular polarization conversion of an electromagnetic wave," *Opt. Mater. Expr.*, vol. 8, no. 3, 2018, Art. no. 597.

[10] B. Lin, L. Lv, J. Guo, Z. Liu, X. Ji, and J. Wu, "An ultra-wideband reflective linear-to-circular polarization converter based on anisotropic metasurface," *IEEE Access*, vol. 8, pp. 82732–82740, 2020.

[11] H. Ma, G. Wang, G. Kong, and T. Cui, "Broadband circular and linear polarization conversions realized by thin birefringent reflective metasurfaces," *Opt. Mater. Expr.*, vol. 4, no. 8, 2014, Art. no. 1717.

[12] Q. Zheng, C. Guo, and J. Ding, "Wideband metasurface-based reflective polarization converter for linear-to-linear and linear-to-circular polarization conversion," *IEEE Antennas Wireless Propag. Lett.*, vol. 17, no. 8, pp. 1459–1463, Aug. 2018.

[13] M. Khan, Z. Khalid, and F. Tahir, "Linear and circular-polarization conversion in X-band using anisotropic metasurface," *Sci. Rep.*, vol. 9, no. 1, 2019, Art. no. 4552.

[14] Q. Zheng, C. Guo, G. Vandenbosch, P. Yuan, and J. Ding, "Dual-broadband highly efficient reflective multi-polarisation converter based on multi-order plasmon resonant metasurface," *IET Microw., Antennas Propag.*, vol. 14, no. 9, pp. 967–972, 2020, doi: 10.1049/iet-map.2019.0984.

[15] H. Yu et al., "Design of a wideband and reconfigurable polarization converter using a manipulable metasurface," *Opt. Mater. Expr.*, vol. 8, no. 11, 2018, Art. no. 3373.

[16] W. Li et al., "A reconfigurable polarization converter using active metasurface and its application in horn antenna," *IEEE Trans. Antennas Propag.*, vol. 64, no. 12, pp. 5281–5290, Dec. 2016.

[17] S. Sun, W. Jiang, S. Gong, and T. Hong, "Reconfigurable linear-to-linear polarization conversion metasurface based on pin diodes," *IEEE Antennas Wireless Propag. Lett.*, vol. 17, no. 9, pp. 1722–1726, Sep. 2018.

[18] X. Gao, W. Yang, H. Ma, Q. Cheng, X. Yu, and T. Cui, "A reconfigurable broadband polarization converter based on an active metasurface," *IEEE Trans. Antennas Propag.*, vol. 66, no. 11, pp. 6086–6095, Nov. 2018.

[19] Y. Li, H. Zhang, T. Yang, T. Sun, and L. Zeng, "A multifunctional polarization converter base on the solid-state plasma metasurface," *IEEE J. Quantum Electron.*, vol. 56, no. 2, 2020, Art. no. 7300107.

[20] Y. Li, H. Li, Y. Wang, Y. Wang, and Q. Cao, "A novel switchable absorber/linear converter based on active metasurface and its application," *IEEE Trans. Antennas Propag.*, vol. 68, no. 11, pp. 7688–7693, Nov. 2020.

[21] Accessed: Jan. 2022. [Online]. Available: http://www.nxp.com/documents/data_sheet/BAP70-03.pdf

[22] S. Bakshi and D. Mitra, "Design and analysis of a bi-functional ground plane with true reconfigurability," *Electron. Lett.*, vol. 55, no. 4, pp. 214–216, 2019.

[23] C. A. Balanis, *Antenna Theory: Analysis and Design*. Hoboken, NJ, USA: Wiley, 2016.

[24] S. Bakshi, D. Mitra, and F. Teixeira, "FSS-based fully reconfigurable rasorber with enhanced absorption bandwidth and simplified bias network," *IEEE Trans. Antennas Propag.*, vol. 68, no. 11, pp. 7370–7381, Nov. 2020.

[25] Q. Guo, Z. Li, J. Su, J. Song, and L. Yang, "Active frequency selective surface with wide reconfigurable passband," *IEEE Access*, vol. 7, pp. 38348–38355, 2019.

[26] M. Karamirad, C. Ghobadi, and J. Nourinia, "Metasurfaces for wideband and efficient polarization rotation," *IEEE Trans. Antennas Propag.,* vol. 69, no. 3, pp. 1799–1804, Mar. 2021.

[27] Z. Yang et al., "Reconfigurable multifunction polarization converter integrated with PIN diode," *IEEE Microw. Wireless Compon. Lett.,* vol. 31, no. 6, pp. 557–560, Jun. 2021.

[28] J. Jiang, J. Kim, A. Karsilayan, and J. Silva-Martinez, "A 3–6 GHz highly linear I-channel receiver with over +3.0-dBm in-band P1dB and 200 MHz baseband bandwidth suitable for 5G wireless and cognitive radio applications," *IEEE Trans. Circuits Syst. I. Reg. Papers,* vol. 66, no. 8, pp. 3134–3147, Aug. 2019.

[29] D. V. Navarro-Méndez et al., "Wideband double monopole for mobile, WLAN, and C2C services in vehicular applications," *IEEE Antennas Wireless Propag. Lett.,* vol. 16, pp. 16–19, 2017, doi: 10.1109/LAWP.2016.2552398.

[30] S. Roy et al., "Design of a compact multi-element monopulse feed for ground-station satellite tracking applications," *IEEE Antennas Wireless Propag. Lett.,* vol. 18, no. 9, pp. 1721–1725, Sep. 2019.

[31] N. Chahat, J. Sauder, M. Mitchell, N. Beidleman, and G. Freebury, "One-meter deployable mesh reflector for deep-space network telecommunication at X-band and Ka-band," *IEEE Trans. Antennas Propag.*, vol. 68, no. 2, pp. 727–735, Feb. 2020.